Engineered Science
DOI: https://dx.doi.org/10.30919/es1158

Simulation Calculation of Selective Reflective Films based on Metamaterials and Prediction of Color in Light Filter with Machine Learning

Pawinee Xiangtian Gao,[1, 2] Ming Yang,[1, 2,*] Aricson Pereira,[3] Sijie Guo[4] and Hang Zhang[1, 2,*]

Abstract

In this study, we have developed a novel three-layer cylindrical periodic structure utilizing metamaterials, combining a periodic cylindrical arrangement with a Metal-Insulator-Metal (MIM) three-layer configuration. The finite difference time domain method is used to calculate the reflection curve of the structure, and then the color coordinates of the structure under the D65 light source are calculated. We obtain the relationship between the color presented by the structure and the variation of structural size parameters. Then the random forest algorithm is used for machine learning, and a more accurate learning model is obtained. The coefficient of determination R^2 is above 0.98. This result ensures that the random forest algorithm can be used in the calculation of superstructure. The article presents a novel light filter design with tunable color properties and machine learning framework for accurate color predictions based on structural parameters.

Keywords: Metamaterials; Selective reflective films; Machine learning; Light filter.
Received: 22 April 2024; Revised: 03 May 2024; Accepted: 25 May 2024.
Article type: Research article.

1. Introduction

Metamaterial is an artificially made material with special optical properties, usually composed of multiple tiny structures.[1] The size of these tiny structures is much smaller than the wavelength of light waves, so they can control the propagation direction, speed and polarization state of light waves. Metamaterials can be used to manufacture optical devices such as mirrors,[2] lenses,[3] and optical fibers,[4] and to develop optical sensors,[5] optical communications[6] and optical computing.[7] Metamaterials are an interdisciplinary field of materials that play an important role in optics,[8] physics[9] and engineering.[10] Theoretical research[11,12] and experimental verification[13,14] of this microstructure are also research hotspots.

Traditional metamaterials basically use certain metals as media to achieve surface plasmon resonance,[15] thereby realizing the properties of metamaterials. The manipulation of electromagnetic waves by plasmonic structures[16] has been the subject of extensive research, with wavelengths ranging from microwave[17] and terahertz radiation[18] to infrared[19] and visible light.[20] Plasmonic structures have tightly controlled sizes and geometries, allowing the absorption spectrum to be tuned by locally controlling the size of the resonant cavity which determines the resonant frequency.[21] This technology has been used in optics to act as color filters and absorbers in transmission,[22] reflection,[23] and phase-critical optical components.[24]

Metamaterial perfect absorber (MPA) is an important application of metamaterials in optics. Metamaterial absorbers usually consist of a three-layer structure, known as a metal/insulator/metal (MIM) structure.[25] The top layer is composed of periodically arranged metal nanopatterns, such as disk,[26] cross,[27] cube,[28] groove,[29] and triangular pillar.[30] The middle layer and the bottom layer are composed of insulator layers and metal layers. A three-layer structure with gold nanopillars with a period of 340nm as the upper metal

[1] *Institute of Engineering Thermophysics, Chinese Academy of Sciences, Beijing 100190, China.*
[2] *University of Chinese Academy of Sciences, Beijing 100049, China.*
[3] *Advanced Materials Division, Engineered Multifunctional Composites (EMC) Nanotech LLC, Knoxville, TN, 37922, United States of America.*
[4] *Department of Chemical and Biomolecular Engineering, University of Tennesee, Knoxville, TN 37996 United States of America.*
**Email:* yangming@iet.cn (M. Yang); zhanghang@iet.cn (H. Zhang)

layer, SiO_2 and Au as the middle layer and the bottom layer can achieve selective reflection of visible light.[31] By changing the diameter of the gold nanopillars and the thickness of the intermediate silica layer, reflection and transmission of visible light in different wavelength bands can be achieved.

In this study, we fabricated a three-layer periodic pillar structure consisting of Au/SiO_2/Au layers on a silicon substrate to harness plasmonic effects. By changing the thickness of the top layer and the middle layer and the diameter of the pillar structure, we calculate the reflection curve of the plasma in the visible light band under different parameters. With the help of color system knowledge, we calculate the color coordinates corresponding to each reflection curve of plasma under D65 light source. Using structural parameters as independent variables and color coordinates as dependent variables, machine learning was used to establish a prediction model and analyze the accuracy of the model and the impact of each structural parameter on the results.

Machine learning is to automatically analyze and obtain patterns from data, and use the patterns to predict unknown data.[32] We use computers as tools and are committed to simulating human learning methods in real-time and dividing existing content into knowledge structures to effectively improve learning efficiency. Machine learning is a multidisciplinary field that plays an important role in physics,[33] materials,[34] and engineering. At the same time, machine learning can be applied to traditional energy fields[35-37] and new energy technologies.[38,39] Establishing machine learning models can also optimize material properties.[40,41]

Random Forest (RF) is an algorithm that integrates multiple trees through the idea of ensemble learning.[42] It performs classification or regression analysis by building multiple decision trees and combining their outputs. This ensemble learning method can handle high-dimensional data, imbalanced data sets, and missing values, and can evaluate the importance of features. Due to these characteristics, the random forest algorithm has been widely used in various aspects such as statistics,[43] materials science,[44] and biology.[45] This work uses the random forest algorithm to build a machine learning model. Based on the open-source code in the literature,[46] make some changes to the parameters of your own calculation model. In the prediction study of the machine learning model, 80% of the data set was used for training, and 5-fold cross-validation was used for parameter selection during the training process.

2. Modeling

Figure 1 presents a schematic diagram of the model constructed for this study. The model was built and analyzed using Lumerical Finite-Difference Time-Domain (FDTD) software. The base material is silicon (Si), with a columnar structure consisting of gold (Au) layers above and below a SiO_2 layer. The parameters of each layer are taken from the database provided by FDTD. The parameters of Au are taken from Johnson and Christy, and the parameters of Si and SiO_2 are taken from Palik. The period of the cylindrical unit is set to 500 nm, and the thickness of the underlying gold is 100nm. These two parameters remain unchanged. We change the thickness of the upper gold layer, the thickness of the middle layer silica and the diameter of the cylinder unit, and calculate the results under different parameters. The diameter varies from 10-500 nm with a increments of 10nm. Three distinct upper gold layer thicknesses (10 nm, 30 nm, and 50 nm) were selected for the thickness of the upper gold layer, and two parameters of 30 and 50nm were selected for the thickness of the silicon dioxide in the middle layer.

The FDTD method, a prevalent technique for electromagnetic field calculations,[47] was employed in this study. Fig. 2 depicts the model establishment and calculation domain setting in FDTD. The orange box area is the calculation domain. The dimension of the computational domain is 3D, and the simulation time is 5000 fs, and the simulation temperature is 300K. The blank area in the calculation domain is the background material and is set to object defined dielectric. The index of the background material is set to 1, and this means the model is in an air environment. An auto non-uniform mesh with the highest

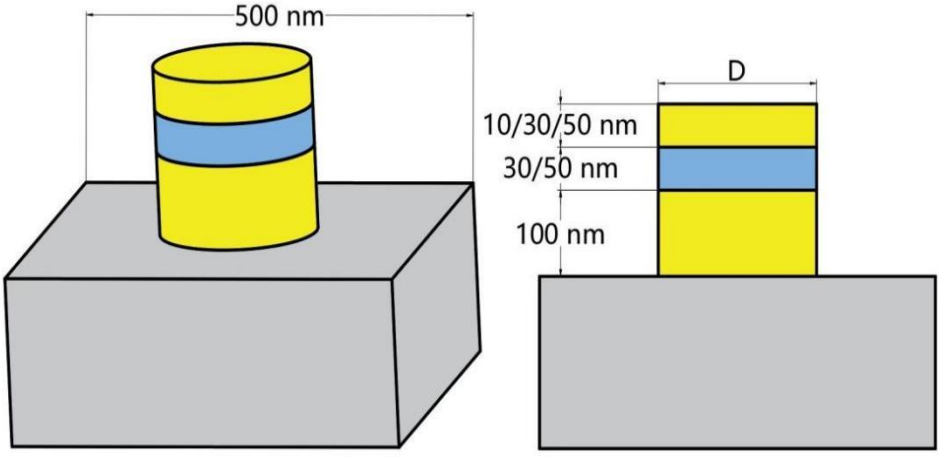

Fig. 1 Schematic diagram of the multi-layer model in this study.

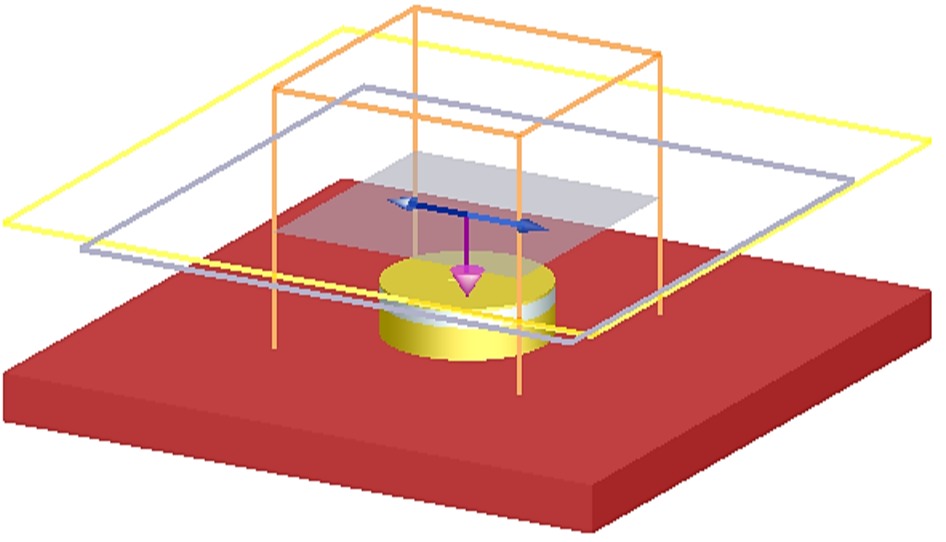

Fig. 2 Model establishment and calculation environment settings.

attainable accuracy level of 8 was implemented, which is the highest accuracy that can be set in FDTD. The min mesh step is 0.25 nm and the stability factor of the time step is 0.99. The boundary conditions in the x and y directions of the computational domain are periodic, which means that the model is a periodic arrangement of the units in the xy plane in the figure. The boundary condition in the z direction of the computational domain is a perfectly matched layer, which means that there are relatively infinitely thick air and silicon above and below the model, respectively.

The light source in this setup is represented by a gray square with an arrow, emitting a plane wave characterized by a Bloch/periodic boundary condition. The light source is a plane wave with a wavelength range of 400-800 nm. Next is the setup of the monitors. The yellow box represents the frequency-domain field and power monitor. The monitor is set to measure the field intensity at 400 frequency points within the 400-800 nm wavelength range. It can receive visible light reflected back by the model and output it in the form of a reflected light intensity curve. In addition, time monitors are installed at a distance of 10 nm from every interface of the model.

3. Result and discussion

According to the knowledge of the color system, the color perceived by the human eye depends on the light source and the object. As shown in Fig. 3, the principle of how we observe objects is that the light emitted by the light source is reflected by the surface of the object and then enters the human eye. Here e is the spectral distribution of the environment, r is the reflection coefficient of the object surface, and l is the light radiation received by the human eye. It can be seen that when we know the spectral distribution of the light source and the reflection curve of the surface of the object being observed, we can obtain the color stimulation function, that is, the light energy that enters the human eye to produce color perception. Color indicators include the well-known GRB system, as well as Lab, XYZ color system, *etc*. Here we use the 1931CIE-XYZ system to digitize the reflection curve obtained. The light source uses D65 light source, which is artificial daylight with a color temperature of 6500K, similar to natural daylight.

Color coordinates XYZ are calculated using the following

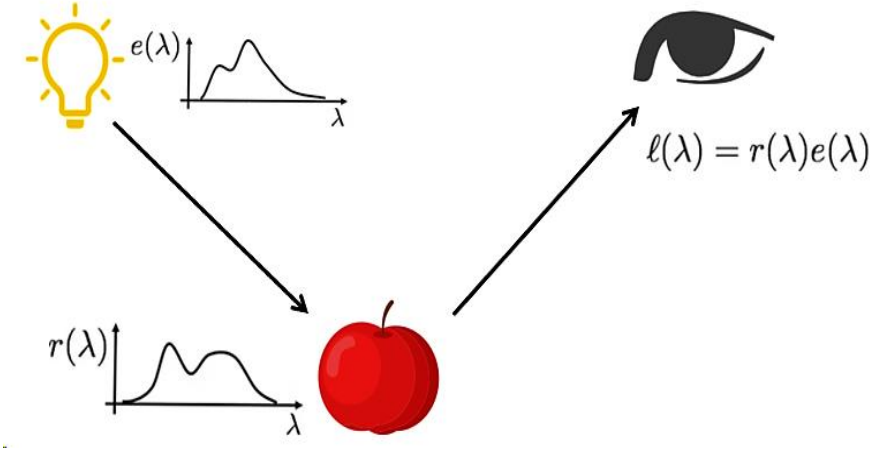

Fig. 3 Principle of object color rendering.

formulae, $X = K\int e(\lambda)\,\bar{x}(\lambda)r(\lambda)d(\lambda)$, $Y = K\int e(\lambda)\,\bar{y}(\lambda)r(\lambda)d(\lambda)$, $Z = K\int e(\lambda)\,\bar{z}(\lambda)r(\lambda)d(\lambda)$. K in the formula is calculated by the following formula, $K = \frac{100}{\int S(\lambda)\bar{y}(\lambda)d(\lambda)}$. $e(\lambda)$ is the relative spectral power distribution of CIE standard light source D65. $\bar{x}(\lambda)$, $\bar{y}(\lambda)$ and $\bar{z}(\lambda)$ are Standard observer tristimulus curve. $r(\lambda)$ is calculated reflectivity of the object at each wavelength. When calculating, the wavelength step $d(\lambda)$ is taken to be 10nm. By getting the color coordinates XYZ of the reflected light of the object under the D65 light source, you can know the color of the object.

Figure 4a shows the reflection curves of periodic column structures with varying diameters when other size parameters (thickness of upper and middle layer) are held consistent. The period is 500 nm, and the thickness of the upper and middle layers is 30 and 20 nm. The diameter selection range is 50-500 nm, and the step size is 50 nm. It can be seen that as the diameter increases, the overall reflection curve first decreases and then increases. In the middle, along with the generation of wave crests and troughs, the wave crest height increases with the increase in diameter. When the diameter is 50 nm, the reflection curve response is basically equivalent to the reflection of visible light by the silicon substrate. As the diameter of the cylinder on the silicon substrate increases, the area of blocked silicon also increases. However, the small-diameter cylindrical structure cannot yet affect the visible light band. Therefore, in the early stage of diameter increase, the reflection curve will first show a downward trend. Then when the diameter increases to a certain value, the structure affects the visible light band, increasing its reflection. This behavior could be due to interplay between increased absorption and resonance effect where with increase in diameter the area of block silicon substrate increases and results in decrease in reflection of light across all spectrums observed. But once structure reaches a certain value it resonates with specific wavelength of visible light and results in increase in reflection of wavelength.

Figure 4b shows the theoretical colors corresponding to the ten diameter parameters in a. The color coordinates XYZ corresponding to the reflection curve are obtained through the formula, and the corresponding color is obtained on the color selection website Colorhexa. It can be found that small change in the diameter of the cylinder increases can significantly change in color of light, the color of the structure gradually becomes brighter from the gray-black color of the silicon substrate itself at the beginning. Fig. 4c shows the distribution of theoretical colors corresponding to ten diameter models in the 1931cie-xy chromatic diagram. Change the color coordinate XYZ to xyY through the following formula, $x = \frac{X}{X+Y+Z}, y = \frac{Y}{X+Y+Z}$. The two parameters x and y represent the chroma of the color, and Y represents the brightness. Subsequent machine learning is also mainly performed on the chromatic coordinate (x, y).

The figures in Fig. 5 illustrate the reflection curves of the model with different silicon dioxide layer thicknesses Fig. 5(a) and different upper gold layer thicknesses Fig. 5(b) when the diameter is 100 nm. It can be observed that as the thickness of the two layers increases, the overall height of the reflection curve does not change significantly. This indicates that the overall reflectance of the light is relatively insensitive to the thickness variations of these layers. Comparatively, the thickness variations in the upper layers exhibit a smaller influence on the reflective properties of the structure. This suggests that though the thickness of these layers might influence the intensity of specific reflected wavelengths, it has a minimal effect on the overall color of the light. Through calculation, these two parameters have little impact on the color coordinates. Through comparison, it can be seen that the

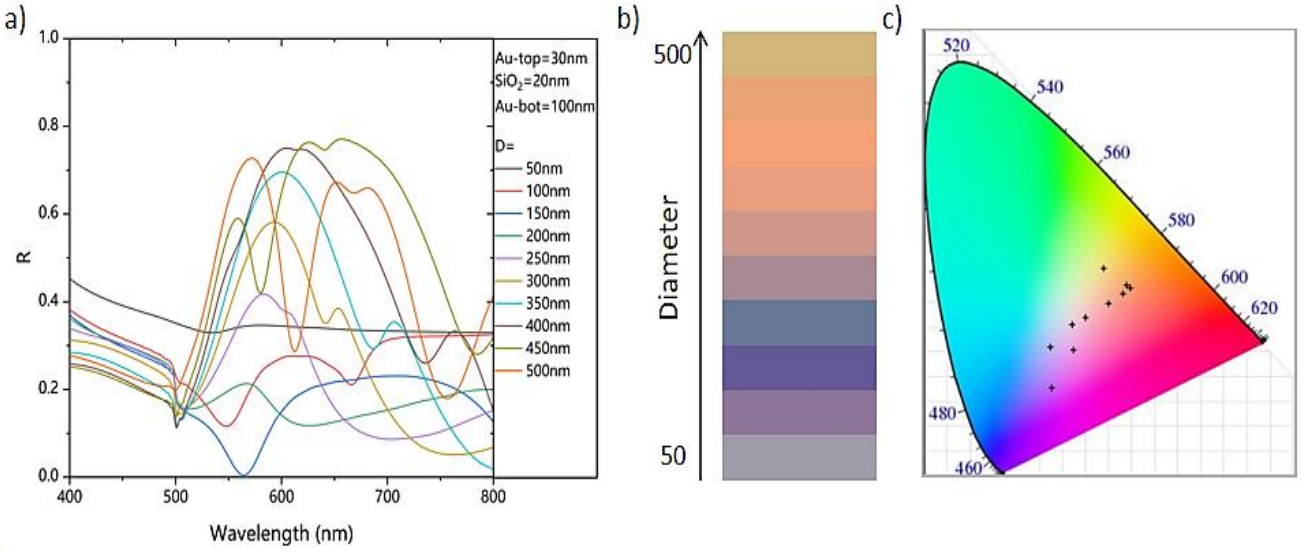

Fig. 4 (a) When the thickness of the upper layer of gold and the thickness of the middle layer of silicon dioxide are 30 and 20nm respectively, calculated reflection curves under different diameter conditions. (b) The theoretical color of the object under the D65 light source under different diameter conditions. (c)The distribution of these ten points on the 1931cie-xy system chromatic diagram.

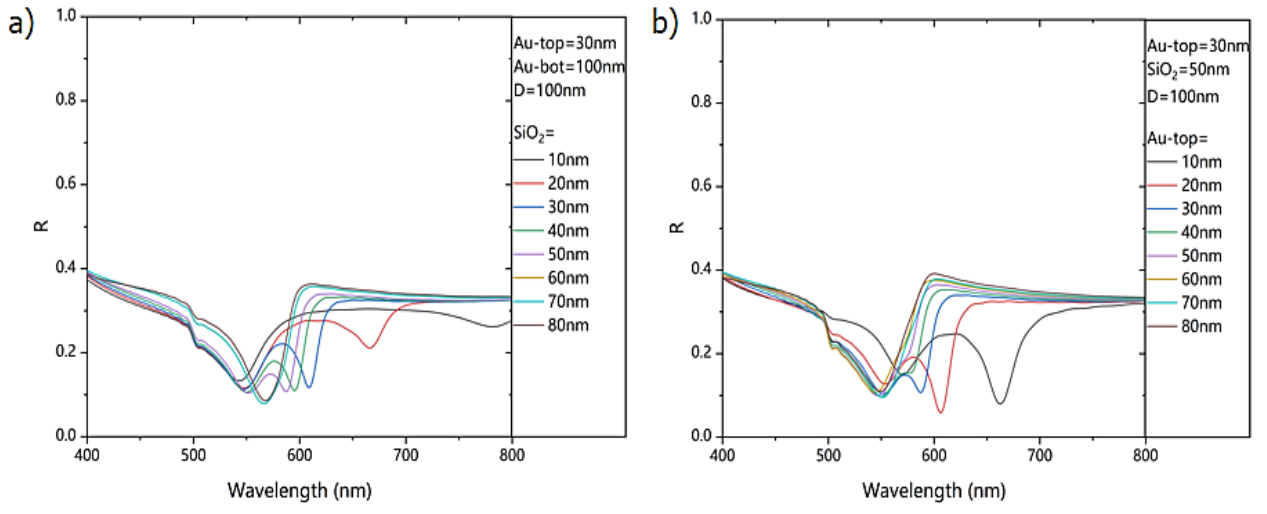

Fig. 5 (a) Reflection curves of models with different silicon dioxide layer thicknesses when the cylinder unit diameter is 100nm. (b) Reflection curves of models with different upper gold layer thicknesses when the cylinder unit diameter is 100nm.

main parameter affecting the reflective performance of the structure is the radius of the periodic structure, and the thickness of the upper two layers has a smaller impact.

4. Machine learning

To construct the dataset required for machine learning, we systematically varied three independent variables: the diameter D of the cylindrical unit, the thickness of the upper gold layer h_1, and the thickness of the middle layer of silicon dioxide h_2. The variation range of D is 10-500 nm, the value of h_1 is 10, 30, 50nm, and the value of h_2 is 20, 50nm. In addition, when the diameter D is 100, 200, 300, and 400nm, the value range of h_1 and h_2 is expanded to 10-100nm (step size is 10nm). For the data set of this study, M = {X， Y}, Y is the calculated color coordinates corresponding to input parameter X (D, h_1 and h_2).

Random forests improve overall prediction performance by constructing multiple individual decision trees. Each decision tree is trained independently by observing features and deciding how to separate the data into different categories or predict numerical values.The core features of the random forest algorithm include: randomness, parallel computing, prevention of overfitting, high accuracy and feature importance. In today's research, random forests can also be combined with classification and regression trees, which have demonstrated powerful results in many fields.[48]

The construction of a machine learning model using the random forest algorithm, as depicted in Fig. 6, involves several key steps.

1) Data Resampling: First, the bootstrap resampling method is used to randomly generate an n-tree data set from the data set M. It is important to create n-copies of original data set to crate diverse training environments.

2) Training and Testing: Subsequently, the data sheet is divided further to 80% of each data set is the training set and 20% is the test set. Following this, n-tree decision trees will be grown on the n-tree data set. The training dataset will build the decision tree and testing data set will check model performance.

3) Model building: Based on the randomness of the algorithm, multiple decision tree are grown by varying diameter and

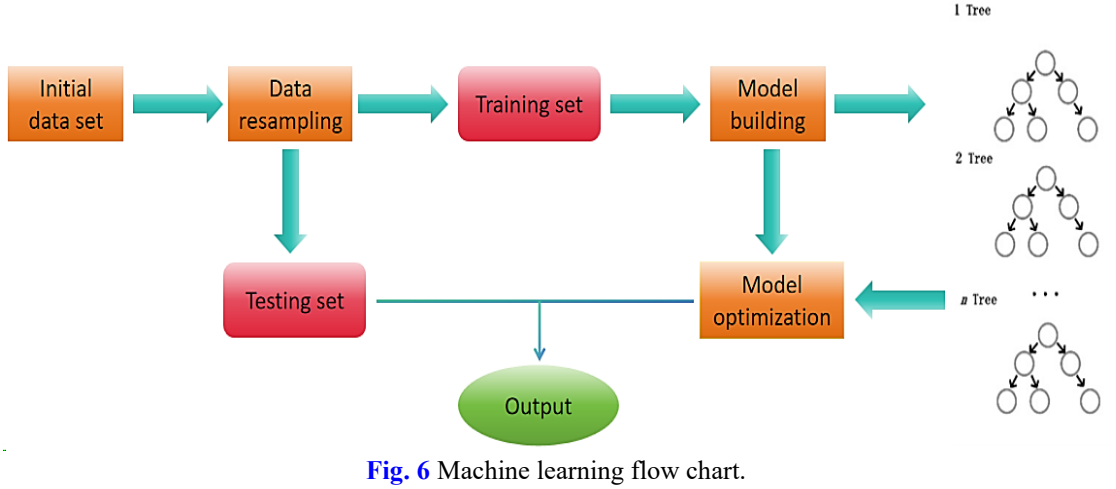

Fig. 6 Machine learning flow chart.

thickness, each decision tree is different, which also ensures the integration performance of the final forest.

4) Model optimization: Finally, Bayesian optimization is leveraged to automatically fine-tune the hyper-parameters of the model.[49] This ensures model performs at its best.

To assess the accuracy of out random forest model, this study employs four widely accepted statistical criteria to evaluate the prediction performance of the model: mean absolute error (MAE), mean absolute percentage error (MAPE), mean square error (MSE), and coefficient of determination (R2). Minimizing MAE, MAPE, and MSE indicates a more accurate model, while an R^2 value approaching 1 signifies a stronger correlation between predicted and actual values. The calculation formulas used to calculate these metrics are shown in Table 1.

Table 1. Calculation formulas of statistical criteria.

Evaluation indicators	Expression
Mean absolute error (MAE)	$MAE = \frac{1}{n}\sum_{i=1}^{n}\lvert f_i - y_i\rvert$
Mean absolute percentage error (MAPE)	$MAPE = \frac{1}{n}\sum_{i=1}^{n}\lvert\frac{f_i - y_i}{y_i}\rvert \times 100\%$
Mean square error (MSE)	$MSE = \frac{1}{n}\sum_{i=1}^{n}(f_i - y_i)^2$
Determination coefficient (R^2)	$R^2 = 1 - \frac{\sum_1^n (y_i - f_i)^2}{\sum_1^n (y_i - \bar{y})^2}$

Table 2. Prediction performance of evaluation indicators.

Models		Evaluation indicators			
		MAE	MAPE(%)	MSE	R^2
x	training	0.0024	0.69	0.000013	0.997
	testing	0.006	1.79	0.000081	0.981
y	training	0.0015	0.52	0.0000046	0.999
	testing	0.004	1.52	0.000035	0.989

The machine learning model was trained to predict two color coordinates (x and y) of light filters. The machine learning process is performed twice for x and y respectively both with training dataset and testing dataset. The coefficient of determination R^2 was used as statistical metric for predicting the accuracy. For the x coordinate, the coefficient of determination R^2 for the training and test sets are 0.997 and 0.981 respectively. Similarly, for the y coordinate, the R^2 for the training and test sets are 0.999 and 0.989. Table 2 shows high R^2 value > 0.98, indicating that the learning models of the two-color coordinates have strong accuracy. This indicates a strong correlation between the predicted and actual color coordinates, suggests machine learning model performs well in predicting the colors of the light.

Figure 7 visualizes the distribution of each data within the model. The horizontal and vertical coordinates are the true value and the predicted value of the model respectively. The closer the point is to the y = x curve in the graph, the more accurate the prediction of the value. This observation is further supported by the absolute percentage error (APE) shown in Fig. 8. The relative error of most points remains within 5%. This further signify good model performance.

It was also noted from Fig. 7 and 8 that absolute percentage error (APE) is centered around 0% error with slight positive skew means that model might slightly overestimating the color coordinates in few instances. This aligns with the observation in Fig. 7 where most points are concentrated in y = x line but the cluster seems to be weak at higher true color coordinates suggested model might be slightly less accurate at higher color coordinates.

The results presented in Fig. 9 demonstrate that, the thickness of two layers among the three selected independent variables exerts a negligible influence on the color coordinates of the final structure. In contrast, the most important parameter is the diameter of the periodic cylindrical element, accounting for 92.83% and 94.32% respectively. This finding suggests that, when other parameters remain unchanged, altering the cylinder diameter can induce a more pronounced shift in the final color.

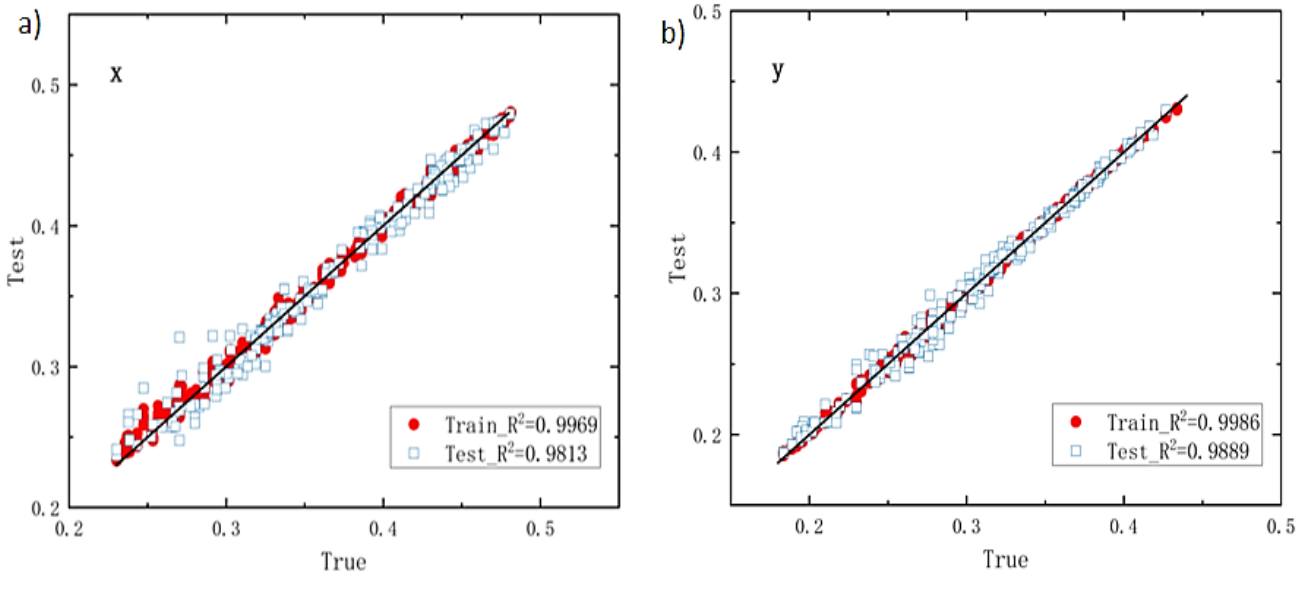

Fig. 7 Prediction results of x and y.

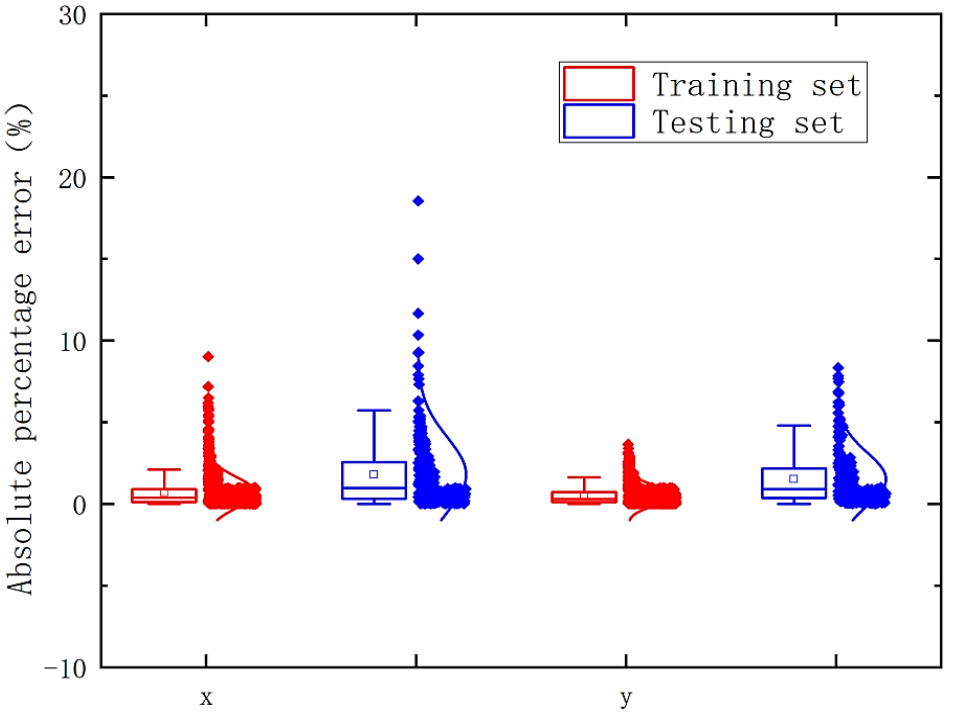

Fig. 8 Absolute percentage error of x and y.

5. Other calculations

For the above model, we also made some other calculations. What we calculated above is the reflection of the model in the visible light band under smaller size parameters. We found that by increasing the size, period and other parameters of the model, the model can be controlled in the infrared band. For example, when the thickness of the three layers in the model is 300nm, the radius is 1200 nm, and the period is 1500 nm, the reflection curve is as shown in Fig. 10. There is a lower reflectivity at 2400 nm and a reflectivity above 90% from 2700 to 4000 nm. This shows that this model also has great potential in infrared control applications by manipulating physical parameters.

In addition to changing the model size parameters, you can also change the shape of the model itself based on the cylindrical structure, such as changing the cylindrical shape to a ring-cylindrical shape. As shown in the Fig. 11, change the model to a ring-cylindrical structure with an inner radius half the outer radius. We calculated the reflectivity of the structure under different radii and compared it with the cylindrical structure under the same parameters, and obtained the curve on the right. Under different wavelength bands of visible light, compared with the columnar structure, the reflectivity of the ring-column structure is enhanced and weakened.

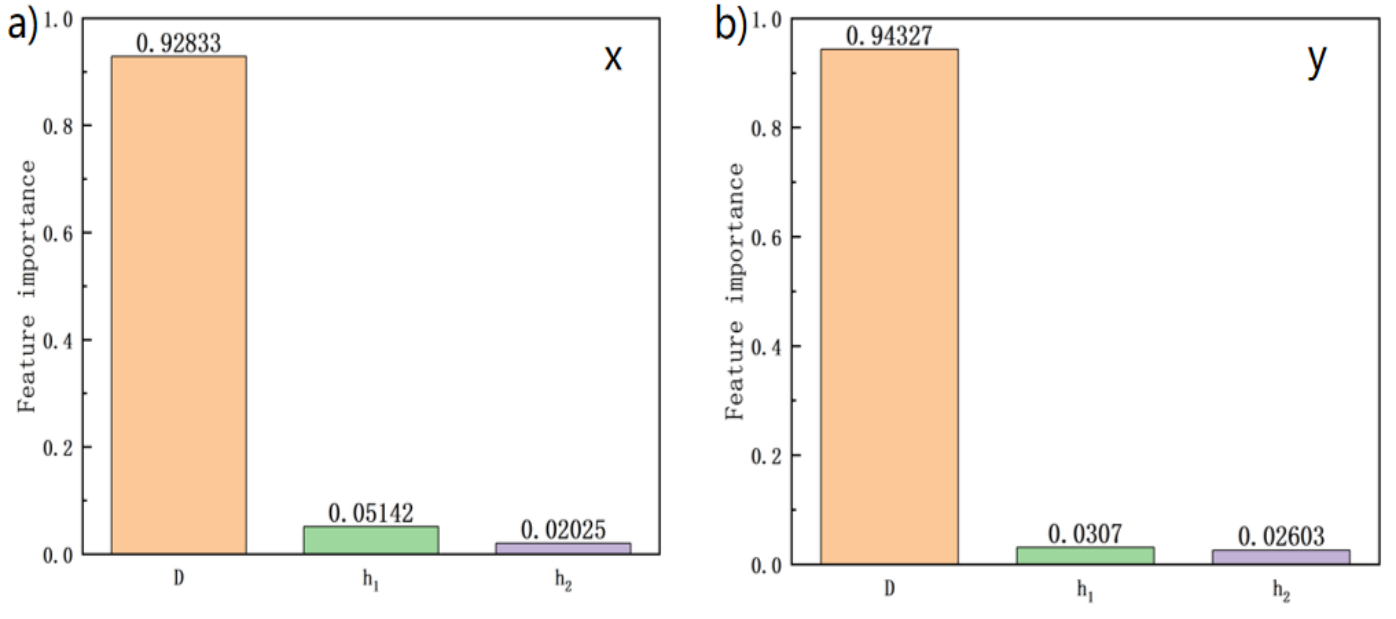

Fig. 9 Results of feature importance, which shows the diameter of the periodic cylindrical element is the most influential parameter.

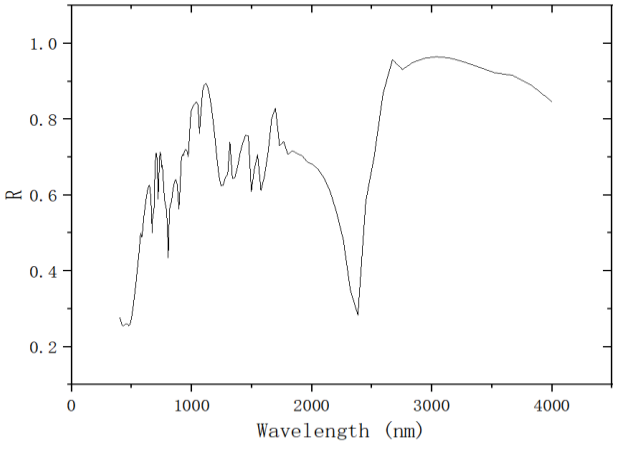

Fig. 10 Control of the infrared band by the structure of large-scale parameters.

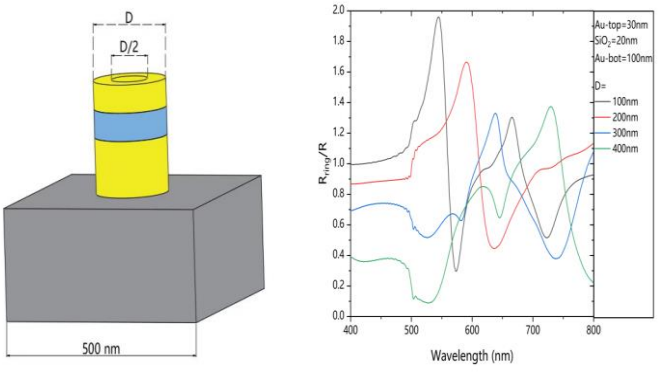

Fig. 11 Derived structures based on the original structure and comparison of reflectance with the original structure.

6. Conclusion

This study investigates the optical properties of a novel surface plasmon structure composed of periodic cylinders coupled with a metal-insulator-metal (MIM) three-layer configuration. The FDTD method was employed to calculate the reflection spectrum of the structure within the visible light band. Subsequently, with the help of relevant knowledge of the color system, the computed reflection curves were translated into corresponding color coordinates under a defined light source. By systematically varying specific structural size parameters, different colors can be obtained with a wide range of color distribution. The comprehensive set of calculated results was then compiled into a dataset and utilized for machine learning via the random forest algorithm. The resulting model exhibited high accuracy, with the cylinder diameter identified as the most influential parameter among the three independent variables considered.

This structure presents opportunities for further computational investigations. Future studies could explore the effects of varying material types and adjusting structural parameters. The larger the amount of data calculated, the higher the accuracy of machine learning specially at higher color wavelengths. Later, a data set for this structure can also be established to implement the function of inputting the target color and obtaining the corresponding structural parameters.

Acknowledgements

This work is supported by the Basic Science Center Program for Ordered Energy Conversion of the National Natural Science Foundation of China (No. 51888103, 51606192 and 52306018) and the CAS Pioneer Hundred Talents Program.

Conflict of Interest

There is no conflict of interest.

Supporting Information

Not applicable.

References

[1] R. S. Kshetrimayum, A brief intro to metamaterials, *IEEE potentials*, 2004, **23**, 44-46, doi: 2003.10.1109/mp.2005.1368916.

[2] J. Rui, D. Wei, A. Rubio-Abadal, S. Hollerith, J. Zeiher, D. M. Stamper-Kurn, C. Gross, I. Bloch, A subradiant optical mirror formed by a single structured atomic layer, *Nature*, 2020, **583**, 369–374, doi: 10.1038/s41586-020-2463-x.

[3] M. Khorasaninejad, W. T. Chen, R. C. Devlin, J. Oh, A. Y. Zhu, F. Capasso, Metalenses at visible wavelengths: Diffraction-limited focusing and subwavelength resolution imaging, *Science*, 2016, **352**, 1190-1194, doi: 10.1126/science.aaf6644.

[4] Y. Yan, H. Ma, L. Wang, H. Li, Z. Jin, Effect of Fresnel reflections in a hybrid air-core photonic-bandgap fiber ring-resonator gyro, *Optics Express*, 2015, **23**, 31384-31392, doi: 10.1364/oe.23.031384.

[5] Z. Yao, X. Xia, Y. Hou, P. Zhang, X. Zhai, Y. Chen, Metasurface-enhanced optical lever sensitivity for atomic force microscopy, *Nanotechnology*, 2019, **30**, 365501, doi: 10.1088/1361-6528/ab2435.

[6] J. Yim, N. Chandra, X. Feng, Z. Gao, S. Wu, T. Wu, H. Zhao, N. M. Litchinitser, L. Feng, Broadband continuous supersymmetric transformation:a new paradigm for transformation optics, *eLight*, 2022, **2**, 16, doi: 10.1186/s43593-022-00023-1.

[7] G. Xu, A bridge between acoustic metamaterials and quantum computation, *Science China Physics, Mechanics & Astronomy*, 2022, **65**, 240331, doi: 10.1007/s11433-022-1856-6.

[8] A. Urbas, Z. Jacob, L. D. Negro, N. Engheta, A. Boardman, P. Egan, A. Khanikaev, V. Menon, M. Ferrera, N. Kinsey, C. DeVault, J. Kim, V. Shalaev, A. Boltasseva, J. Valentine, C. Pfeiffer, A. Grbic, E. Narimanov, L. Zhu, S. Fan, A. Alú, E. Poutrina, N. Litchinitser, M. Noginov, K. Macdonald, E. Plum, X. Liu, P. Nealey, C. Kagan, C. Murray, D. Pawlak, I. Smolyaninov, V. Smolyaninova, D. Chanda, Roadmap on optical metamaterials, *Journal of Optics*, 2016, **18**, 093005, doi: 10.1088/2040-8978/18/9/093005.

[9] E. Barchiesi, M. Spagnuolo, L. Placidi, Mechanical metamaterials: a state of the art, *Mathematics and Mechanics of Solids*, 2019, **24**, 212-234, doi:

10.1177/1081286517735695.
[10] L. Feng, P. Huo, Y. Liang, T. Xu, Photonic metamaterial absorbers: morphology engineering and interdisciplinary applications, *Advanced Materials*, 2020, **32**, 1903787, doi: 10.1002/adma.201903787.
[11] A.-C. Ji, X. C. Xie, W. M. Liu, Quantum magnetic dynamics of polarized light in arrays of microcavities, *Physical Review Letters*, 2007, **99**, 183602, doi: 10.1103/physrevlett.99.183602.
[12] X.-L. Zhang, L.-F. Liu, W.-M. Liu, Quantum anomalous Hall effect and tunable topological states in 3d transition metals doped silicene, *Scientific Reports*, 2013, **3**, 2908, doi: 10.1038/srep02908.
[13] Y.-H. Chen, H.-S. Tao, D.-X. Yao, W.-M. Liu, Kondo metal and ferrimagnetic insulator on the triangular kagome lattice, *Physical Review Letters*, 2012, **108**, 246402, doi: 10.1103/physrevlett.108.246402.
[14] W. Lai, Y.-Q. Ma, L. Zhuang, W. Liu, Photovoltaic effect of atomtronics induced by an artificial gauge field, *Physical Review Letters*, 2019, **122**, 223202, doi: 10.1103/physrevlett.122.223202.
[15] W. Hou, S. B. Cronin, A review of surface plasmon resonance-enhanced photocatalysis, *Advanced Functional Materials*, 2013, **23**, 1612-1619, doi: 10.1002/adfm.201202148.
[16] S. Chen, Z. Li, Y. Zhang, H. Cheng, J. Tian, Phase manipulation of electromagnetic waves with metasurfaces and its applications in nanophotonics, *Advanced Optical Materials*, 2018, **6**, 1800104, doi: 10.1002/adom.201800104.
[17] T. Jiang, L. Shen, J.-J. Wu, T.-J. Yang, Z. Ruan, L. Ran, Realization of tightly confined channel plasmon polaritons at low frequencies, *Applied Physics Letters*, 2011, **99**, doi: 10.1063/1.3672048.
[18] P. Gay-Balmaz, C. Maccio, O. J. F. Martin, Microwire arrays with plasmonic response at microwave frequencies, *Applied Physics Letters*, 2002, **81**, 2896-2898, doi: 10.1063/1.1513663.
[19] Nielsen, R.B., et al., Fabrication of Plasmonic Waveguides by Nanoimprint and UV Lithography. *Proc Spie*, 2008, **6**, 117-126, doi: 10.1117/12.762999.
[20] A. Pors, O. Albrektsen, I. P. Radko, S. I. Bozhevolnyi, Gap plasmon-based metasurfaces for total control of reflected light, *Scientific Reports*, 2013, **3**, 2155, doi: 10.1038/srep02155.
[21] V. Giannini, A. I. Fernández-Domínguez, S. C. Heck, S. A. Maier, Plasmonic nanoantennas: fundamentals and their use in controlling the radiative properties of nanoemitters, *Chemical Reviews*, 2011, **111**, 3888-3912, doi: 10.1021/cr1002672.
[22] Q. Chen, D. R. S. Cumming, High transmission and low color cross-talk plasmonic color filters using triangular-lattice hole arrays in aluminum films, *Optics Express*, 2010, **18**, 14056, doi: 10.1364/oe.18.014056.
[23] J. Zhang, K. F. MacDonald, N. I. Zheludev, Giant optical forces in planar dielectric photonic metamaterials, *Optics Letters*, 2014, **39**, 4883-4886, doi:10.1364/ol.39.004883.
[24] A. Pors, M. G. Nielsen, G. Della Valle, M. Willatzen, O. Albrektsen, S. I. Bozhevolnyi, Plasmonic metamaterial wave retarders in reflection by orthogonally oriented detuned electrical dipoles, *Optics Letters*, 2011, **36**, 1626, doi: 10.1364/ol.36.001626.
[25] G. Liu, X. Liu, J. Chen, Y. Li, L. Shi, G. Fu, Z. Liu, Near-unity, full-spectrum, nanoscale solar absorbers and near-perfect blackbody emitters, *Solar Energy Materials and Solar Cells*, 2019, **190**, 20-29, doi: 10.1016/j.solmat.2018.10.011.
[26] N. Liu, M. Mesch, T. Weiss, M. Hentschel, H. Giessen, Infrared perfect absorber and its application as plasmonic sensor, *Nano Letters*, 2010, **10**, 2342-2348, doi: 10.1021/nl9041033.
[27] S. Kang, Z. Qian, V. Rajaram, S. D. Calisgan, A. Alù, M. Rinaldi, Ultra-narrowband metamaterial absorbers for high spectral resolution infrared spectroscopy, *Advanced Optical Materials*, 2019, **7**, 1801236, doi: 10.1002/adom.201801236.
[28] S. Yue, M. Hou, R. Wang, H. Guo, Y. Hou, M. Li, Z. Zhang, Y. Wang, Z. Zhang, Ultra-broadband metamaterial absorber from ultraviolet to long-wave infrared based on CMOS-compatible materials, *Optics Express*, 2020, **28**, 31844, doi: 10.1364/oe.403551.
[29] T. Søndergaard, S. M. Novikov, T. Holmgaard, R. L. Eriksen, J. Beermann, Z. Han, K. Pedersen, S. I. Bozhevolnyi, Plasmonic black gold by adiabatic nanofocusing and absorption of light in ultra-sharp convex grooves, *Nature Communications*, 2012, **3**, 969, doi: 10.1038/ncomms1976.
[30] Y. Li, D. Li, D. Zhou, C. Chi, S. Yang, B. Huang, Efficient, scalable, and high-temperature selective solar absorbers based on hybrid-strategy plasmonic metamaterials (solar RRL 8⁄2018), *Solar RRL*, 2018, **2**, 1870196, doi: 10.1002/solr.201870196.
[31] A. S. Roberts, A. Pors, O. Albrektsen, S. I. Bozhevolnyi, Subwavelength plasmonic color printing protected for ambient use, *Nano Letters*, 2014, **14**, 783-787, doi: 10.1021/nl404129n.
[32] T. M. Mitchell, R. Hutchinson, R. S. Niculescu, F. Pereira, X. Wang, M. Just, S. Newman, Learning to decode cognitive states from brain images. Machine learning, 2004, **57**, 145-175, doi: 10.1023/b:mach.0000035475.85309.1b.
[33] C. Yu, X. Zhu, Z. Li, Y. Ma, M. Yang, H. Zhang, Optimization of elliptical pin-fin microchannel heat sink based on artificial neural network, *International Journal of Heat and Mass Transfer*, 2023, **205**, 123928, doi: 10.1016/j.ijheatmasstransfer.2023.123928.
[34] Y.-C. Hu, Data-driven prediction of the glass-forming ability of modeled alloys by supervised machine learning, *Journal of Materials Informatics*, 2023, **3**, 1, doi: 10.20517/jmi.2022.28.
[35] Z. Zheng, X. Lin, M. Yang, Z. He, E. Bao, H. Zhang, Z. Tian, Progress in the application of machine learning in combustion studies, *ES Energy & Environment*, 2020, **9**, 1-14, doi: 10.30919/esee8c795.
[36] Z. Chen, F. Vom Lehn, H. Pitsch, L. Cai, Prediction of

sooting index of fuel compounds for spark-ignition engine applications based on a machine learning approach, *Journal of Thermal Science*, 2023, **32**, 521-530, doi: 10.1007/s11630-023-1765-3.
[37] H. Zhou, K. Yu, Q. Luo, L. Luo, W. Du, S. Wang, Design methods and strategies for forward and inverse problems of turbine blades based on machine learning, *Journal of Thermal Science*, 2022, **31**, 82-95, doi: 10.1007/s11630-022-1544-6.
[38] Z. He, M. Yang, L. Wang, E. Bao, H. Zhang, Concentrated photovoltaic thermoelectric hybrid system: an experimental and machine learning study, *Engineered Science*, 2021, **15**, 47-56, doi: 10.30919/es8d440.
[39] Z. Wang, M. Yang, X. Xie, C. Yu, Q. Jiang, M. Huang, H. Algadi, Z. Guo, H. Zhang, Applications of machine learning in perovskite materials, *Advanced Composites and Hybrid Materials*, 2022, **5**, 2700-2720, doi: 10.1007/s42114-022-00560-w.
[40] A. K. Y. Low, E. Vissol-Gaudin, Y.-F. Lim, K. Hippalgaonkar, Mapping Pareto fronts for efficient multi-objective materials discovery, *Journal of Materials Informatics*, 2023, **3**, 11, doi: 10.20517/jmi.2023.02.
[41] S. S. Omee, L. Wei, M. Hu, J. Hu, Crystal structure prediction using neural network potential and age-fitness Pareto genetic algorithm, *Journal of Materials Informatics*, 2024, **4**, 2, doi: 10.20517/jmi.2023.33.
[42] L. Breiman, Random forests, machine learning 45, *Journal of Clinical Microbiology*, 2001, **2**, 199-228.
[43] Y. Wang, Y. Li, W. Pu, K. Wen, Y. Y. Shugart, M. Xiong, L. Jin, Random bits forest: a strong classifier/regressor for big data, *Scientific Reports*, 2016, **6**, 30086, doi: 10.1038/srep30086.
[44] J. Carrete, W. Li, N. Mingo, S. Wang, S. Curtarolo, Finding unprecedentedly low-thermal-conductivity half-heusler semiconductors via high-throughput materials modeling, *Physical Review X*, 2014, **4**, 011019, doi: 10.1103/physrevx.4.011019.
[45] C. Maltecca, D. Lu, C. Schillebeeckx, N. P. McNulty, C. Schwab, C. Shull, F. Tiezzi, Predicting growth and carcass traits in swine using microbiome data and machine learning algorithms, *Scientific Reports*, 2019, **9**, 6574, doi: 10.1038/s41598-019-43031-x.
[46] Y. Wang, A. W. Kandeal, A. Swidan, S. W. Sharshir, G. B. Abdelaziz, M. A. Halim, A. E. Kabeel, N. Yang, Prediction of tubular solar still performance by machine learning integrated with Bayesian optimization algorithm, *Applied Thermal Engineering*, 2021, **184**, 116233, doi: 10.1016/j.applthermaleng.2020.116233.
[47] K. Yee, Numerical solution of initial boundary value problems involving Maxwell's equations in isotropic media, *IEEE Transactions on Antennas and Propagation*, 1966, **14**, 302-307, doi: 10.1109/TAP.1966.1138693.
[48] D. S. Palmer, N. M. O'Boyle, R. C. Glen, J. B. O. Mitchell, Random forest models to predict aqueous solubility, *Journal of Chemical Information and Modeling*, 2007, **47**, 150-158, doi: 10.1021/ci060164k.
[49] A. Kenny, T. Ray, S. Limmer, H. K. Singh, T. Rodemann, M. Olhofer, Hybridizing TPOT with Bayesian optimization. *InProceedings of the Genetic and Evolutionary Computation Conference*, 2023, **15**, 502-510, doi: 10.1145/3583131.3590364.

